

# Journal Pre-proof

Initial investigation of B<sub>4</sub>C–TiB<sub>2</sub> composites as neutron absorption material for nuclear reactors

Ji Wang, Donglou Ren, LeiLei Chen, Guian Man, Houyuan Zhang, Hongpeng Zhang, Laihui Luo, Weiping Li, Yanbo Pan, Peifeng Gao, Yabin Zhu, Zhiguang Wang

PII: S0022-3115(20)30456-6

DOI: <https://doi.org/10.1016/j.jnucmat.2020.152275>

Reference: NUMA 152275

To appear in: *Journal of Nuclear Materials*

Received Date: 25 March 2020

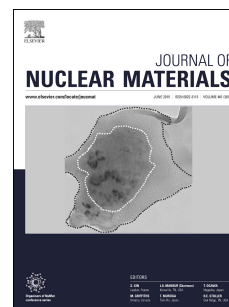
Revised Date: 28 May 2020

Accepted Date: 28 May 2020

Please cite this article as: J. Wang, D. Ren, L. Chen, G. Man, H. Zhang, H. Zhang, L. Luo, W. Li, Y. Pan, P. Gao, Y. Zhu, Z. Wang, Initial investigation of B<sub>4</sub>C–TiB<sub>2</sub> composites as neutron absorption material for nuclear reactors, *Journal of Nuclear Materials* (2020), doi: <https://doi.org/10.1016/j.jnucmat.2020.152275>.

This is a PDF file of an article that has undergone enhancements after acceptance, such as the addition of a cover page and metadata, and formatting for readability, but it is not yet the definitive version of record. This version will undergo additional copyediting, typesetting and review before it is published in its final form, but we are providing this version to give early visibility of the article. Please note that, during the production process, errors may be discovered which could affect the content, and all legal disclaimers that apply to the journal pertain.

© 2020 Published by Elsevier B.V.



**Ji Wang:** Conceptualization, Methodology, Investigation, Writing – original draft, Writing - review & editing, Visualization. **Donglou Ren:** Methodology, Investigation, Writing – original draft, Writing - review & editing, Visualization. **LeiLei Chen:** Investigation, resources. **Guian Man:** Writing - review & editing, software. **Houyuan Zhang:** Writing - review & editing, software. **Hongpeng Zhang:** Investigation, resources. **Laihui Luo:** Conceptualization. **Weiping Li:** Conceptualization. **Yanbo Pan:** Resources. **Peifeng Gao:** Conceptualization, Methodology, Writing - review & editing, software, Funding acquisition, Supervision. **Yabin Zhu:** Conceptualization, Methodology, Writing - review & editing, resources, Supervision. **Zhiguang Wang:** Conceptualization, Methodology, Supervision, Funding acquisition.

# **Initial investigation of B<sub>4</sub>C–TiB<sub>2</sub> composites as neutron absorption material for nuclear reactors**

Ji Wang<sup>a, 1</sup>, Donglou Ren<sup>b, 1</sup>, LeiLei Chen<sup>c</sup>, Guian Man<sup>d</sup>, Houyuan Zhang<sup>d</sup>,  
Hongpeng Zhang<sup>e</sup>, Laihui Luo<sup>a</sup>, Weiping Li<sup>a</sup>, Yanbo Pan<sup>a</sup>, Peifeng Gao<sup>d, \*</sup>,  
Yabin Zhu<sup>e, \*</sup>, Zhiguang Wang<sup>e, \*</sup>

<sup>a</sup>School of Physical Science and Technology, Ningbo University, Ningbo  
315211, China

<sup>b</sup>ISCR (Institut des Sciences Chimiques de Rennes)-CNRS, UMR 6226,  
Univ. Rennes, F-35000, Rennes, France

<sup>c</sup>Ningbo Institute of Materials Technology and Engineering, Chinese  
Academy of Sciences, Ningbo, 315201, China

<sup>d</sup>Key Laboratory of Mechanics on Western Disaster and Environment,  
Ministry of Education, College of Civil Engineering and Mechanics,  
Lanzhou University, Lanzhou 730000, China

<sup>e</sup>Institute of Modern Physics, Chinese Academy of Sciences, Lanzhou  
730000, China

\* Corresponding Authors: gaopf@lzu.edu.cn, zhuyabin@impcas.ac.cn,  
zhgwang@impcas.ac.cn

<sup>1</sup> Ji Wang and Donglou Ren contributed equally to this work.

## 23 Abstract

24 In this study, a specifically designed  $B_4C$ - $TiB_2$  composite with the  
25 typical microstructural feature of a  $TiB_2$  network (cages) that  
26 encapsulates a  $B_4C$  matrix was fabricated by the molten-salt and spark  
27 plasma sintering (SPS) method. The finite-element (FE) calculation  
28 results show that the connected  $TiB_2$  cages constitute a thermally  
29 conductive network, which effectively improves the overall thermal  
30 conductivity of the composite; these results agree well with the  
31 experimental results. Moreover, the Vickers indentation results reveal that  
32 the  $TiB_2$  network (cages) can effectively impinge/block the propagation  
33 of cracks, which increases the composite toughness. The composite was  
34 subjected to helium (He) ion irradiation to simulate the situation in which  
35 the  $B_4C$ - $TiB_2$  composites serve as neutron absorption material, and for  
36 which case a high quantity of He atoms is produced by the  $B^{10}(n, \alpha) Li^7$   
37 nuclear reaction. According to the transmission electron microscopy  
38 (TEM) results, the interfaces between  $TiB_2$  and  $B_4C$  act as effective sinks  
39 for He atoms, and are preferential nucleation sites for He bubbles. The  
40 theoretical and experimental results show that when the  $B_4C$ - $TiB_2$   
41 composites serve as neutron absorption pellets in nuclear reactors, they  
42 exhibit a better resistance to their disintegration than pure  $B_4C$  pellets.  
43 Consequently, the performance of the control rods of nuclear reactors can  
44 be improved.

45 Keywords: neutron absorber;  $B_4C$  pellet; He irradiation; crack  
46 propagation; finite element.

47

Journal Pre-proof

## 1. Introduction

$B_4C$  is widely used as a neutron absorption material for control rods (CRs) in many nuclear reactor systems, in particular in fast reactor systems [1] (e.g., Phenix (France), BN (Russia), JOYO (Japan), ALMR, FFTF (United States)) owing to its high melting temperature, outstanding thermal stability, good mechanical properties, and the high neutron absorption cross section of  $^{10}B$ ;  $B_4C$  neutron absorbers play an important role regarding the performance of CRs by, for example, adjusting the reactivity compensation during the normal operation cycles of nuclear reactors, initiating/terminating an operation cycle for refueling or reactor component maintenance, and rapidly shutting down the reactor if abnormal conditions occur. Therefore,  $B_4C$  neutron absorbers are of primary importance for the safe and efficient operation of nuclear reactors.

In many CR designs (e.g., JOYO),  $B_4C$  materials are usually presented in the form of pellets. However, during the operation lifetime of CRs,  $B_4C$  pellets often fracture into pieces and even powders [2]. These fractured  $B_4C$  pellet pieces progressively fill the gaps between the pellets and cladding materials, which accelerates the absorber-cladding mechanical interaction [2]. This leads to an incompatibility between the cladding materials and other components of reactors (e.g., induced absorber swelling cladding cracking (IASCC)) and shortens the CR

lifetime. Moreover, the cracked materials are very sensitive to the subsequent radiation-assisted dissolution (i.e., radiolysis effects [3-5]). Regarding water-cooled nuclear systems, when cooling water leaks into the pellet capsule owing to IASCC-induced cracking [6], the radiolysis effect accelerates the dissolution of the absorber materials and promotes the disintegration of  $B_4C$  pellets [5]. Both effects degrade the CRs and safe operation of nuclear reactors.

According to previous research studies, the disintegration of bulk  $B_4C$  ceramic pellets is closely associated with the thermal-gradient-induced macrocracks and swelling-gradient-induced microcracks [7]. During the service lifetime of CRs, the  $(n, \alpha)$  nuclear reaction releases an average energy of 2.78 MeV per event [1]; the most energy is deposited within the  $B_4C$  matrix. For instance, at a CR burnup of  $10^{22}$  cap/cm<sup>3</sup> per year, a volume power of  $1.5 \times 10^2$  W/cm<sup>3</sup> is deposited in the  $B_4C$  pellets. Owing to the low thermal conductivity of  $B_4C$  and the high heat-generation rate caused by the  $^{10}B (n, \alpha) ^7Li$  reaction, the temperature gradient of  $B_4C$  pellets can reach up to  $10^3$  K/cm. Such a high temperature gradient causes a great thermal stress and results in thermal-stress-induced macrocracks. Moreover, a high quantity of He atoms produced by the transmutation reaction accumulate in the form of flat lenticular He bubbles [8,9]. These He bubbles cause significant volume swelling. When the neutron absorption pellets are placed in

thermal neutron reactors, owing to the self-shielding effect [7,10], the burnup of the pellet periphery is usually stronger than that of the interior. Because the He atom production is proportional to the burnup level, a gradient distribution of He bubbles leads to a steep swelling gradient of the B<sub>4</sub>C material and an abrupt local strain [7]: the consequence are swelling-gradient-induced microcracks. In general, the released heat and He atoms produced by the  $^{10}\text{B} (n, \alpha) ^7\text{Li}$  reaction are two factors that lead to the formation of cracks. Both factors promote the formation of macro-scale cracks and facilitate the crack propagation through pellets, which result in their disintegration [2,11].

Therefore, it is of vital importance to improve the thermal conductivity and irradiation-induced swelling resistance of B<sub>4</sub>C absorber materials to guarantee the good long-term performance of CRs and a safe and efficient operation of nuclear reactors. B<sub>4</sub>C–diborides composites have been explored a long time ago to improve the performance of B<sub>4</sub>C in the irradiation field. For example, B<sub>4</sub>C–HfB<sub>2</sub> composite was designed to improve fracture toughness [12, 13] and the thermal-mechanical properties of the neutron absorber [12]. In this study, a low economic cost and honeycomb-structured B<sub>4</sub>C–TiB<sub>2</sub> composite was elaborated to attain the aforementioned objective. The main feature of the composite is a highly thermally conductive cage-like TiB<sub>2</sub> network that encapsulates conventional B<sub>4</sub>C matrix grains. TiB<sub>2</sub> has a high melting point (3498 K),



exceptional hardness (25-35 GPa), highly thermal conductivity, excellent wear resistance, a low thermal expansion coefficient ( $4.6 \times 10^{-6} \text{ K}^{-1}$ , which is almost the same as that of  $\text{B}_4\text{C}$ ,  $4.5 \times 10^{-6} \text{ K}^{-1}$ ), and a high oxidation resistance [14-18]. Owing to the inimitable characteristics of  $\text{TiB}_2$ , it is therefore selected as the cage-like structure of the  $\text{B}_4\text{C}$ – $\text{TiB}_2$  composites. The good features of conventional  $\text{B}_4\text{C}$  material are maintained, and the thermal conductivity of the composite is significantly improved with respect to that of the pure  $\text{B}_4\text{C}$  material. In addition, the composite exhibits many interfaces.

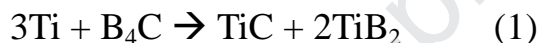
The  $\text{B}_4\text{C}$ – $\text{TiB}_2$  composites were subjected to He ion irradiation to simulate the situation in which the  $\text{B}_4\text{C}$ – $\text{TiB}_2$  composite is exposed to a high neutron flux, and a high quantity of He atoms is produced by the (n,  $\alpha$ ) reaction. Moreover, a series of post-irradiation analyses and FE calculations were conducted to evaluate the behavior of the  $\text{B}_4\text{C}$ – $\text{TiB}_2$  component in a nuclear reactor environment.

## 2. Experimental details

### 2.1. Material synthesis

A two-step synthesis method was employed to synthesize the  $\text{B}_4\text{C}$ – $\text{TiB}_2$  composite [19]. In the first step, Ti and  $\text{B}_4\text{C}$  powders were mixed with NaCl and KCl in an  $\text{Al}_2\text{O}_3$  crucible. The mixtures with initial  $\text{B}_4\text{C}/\text{Ti}$  molar ratios of 6:1, 4:1, and 2:1 were exposed to an Ar atmosphere at 1273 K. After the (1) and (2) in-situ reactions in the melted salt bath, a

uniform  $\text{TiB}_2$  coating occurred on the  $\text{B}_4\text{C}$  particles. The remnant  $\text{NaCl}$ ,  $\text{KCl}$ , and other impurities were washed away with deionized water, and the samples were subsequently dried to obtain dry  $\text{TiB}_2$ -coated  $\text{B}_4\text{C}$  powders. Note that the melt point of  $\text{NaCl}$  and  $\text{KCl}$  mixing is low ( $\sim 933$  K) and the liquid mass transfer mode between  $\text{B}_4\text{C}$  and  $\text{Ti}$  in the molten salts guarantees the uniform nucleation and growth of  $\text{TiB}_2$  on the surface of  $\text{B}_4\text{C}$  particles. Therefore, the  $\text{NaCl}$  and  $\text{KCl}$  were employed as the medium for reactions.



In the second step, the mixtures containing uniformly  $\text{TiB}_2$ -coated  $\text{B}_4\text{C}$  powders with different  $\text{TiB}_2$  contents were sintered in a spark plasma sintering (SPS) system (SPS-20T-15, Chen Hua) with the same procedure to obtain three cylindrical bulk samples with diameters of 13 mm and heights of 2 mm (denoted as S1, S2, and S3). In the SPS procedure, the heating rates are 50 K/min from RT to 1673 K, and 25 K/min from 1673 K to 1973 K, respectively. The holding time and temperature are 10 min and 1973 K, respectively. The pressure during the holding stage is 45 MPa. The cooling rate is 50 K/min from the holding temperature to RT. Each bulk sample has a relative density of 100%. The volume fractions of  $\text{TiB}_2$  phases in  $\text{B}_4\text{C}$ - $\text{TiB}_2$  composites are determined by the equation (3).

$$\frac{V_{TiB_2}}{V_t} = \frac{\frac{m_{TiB_2}}{\rho_{TiB_2}}}{\frac{m_t}{\rho_t}} = w_{TiB_2} \cdot \frac{\rho_t}{\rho_{TiB_2}} \quad (3)$$

Where  $V_{TiB_2}$  and  $V_t$  are the volume of  $TiB_2$  phases and the  $B_4C-TiB_2$  composites, respectively.  $w_{TiB_2}$  is the weight percent of  $TiB_2$  measured by using XRD, the calculated weight percent of  $TiB_2$  for S1, S2 and S3 are 18 %, 26% and 44%, respectively.  $\rho_{TiB_2}$  ( $4.5 \text{ g/cm}^3$ ) is the density of  $TiB_2$  and  $\rho_t$  is the density of the  $B_4C-TiB_2$  composites (2.637, 2.796 and  $3.051 \text{ g/cm}^3$  for S1, S2 and S3, respectively). The density of the  $B_4C-TiB_2$  composites were measured by and Archimedes method. The chemical composition and the calculated volume fraction of each sample are shown in Table 1.

## 2.2. Vickers indentation tests and irradiation procedure

A pyramidal diamond tip with an apical angle of  $136^\circ$  was used to perform Vickers indentation tests. The tests were performed on the surface of the virgin samples to investigate the crack propagation behavior in the composite. During the indentation tests, the maximal load was set to 9.8 N, and the holding time was 15 s. Each indentation was set more than  $100 \mu\text{m}$  apart to avoid an overlap of the indentation-induced deformations or crack outspread regions.

The He ion irradiation procedure was conducted in a terminal chamber with a 320 kV multidiscipline research platform for highly

charged ions at the Institute of Modern Physics (IMP), Lanzhou, China. Samples S1, S2, and S3 were irradiated with 500 keV He ions with  $1 \times 10^{17}$  ions/cm<sup>2</sup> at 773 K. After the irradiation process, the samples were annealed at 1273 K for 25 min in a vacuum of  $10^{-5}$  Pa. In addition, Stopping Range of Ions in Matter (SRIM) codes were conducted with the Kinchin–Pease quick-calculation mode to predict the distribution of the He atoms and displacement damage in B<sub>4</sub>C and TiB<sub>2</sub>, respectively. The calculated distribution is a function of the penetration depth, as shown in Fig. 1; the Bragg peak with a He concentration of  $8.92 \times 10^{21}$  cm<sup>-3</sup> (7.02%) is located at a depth of  $\sim 1.38$   $\mu$ m in the B<sub>4</sub>C material, and  $7.18 \times 10^{21}$  cm<sup>-3</sup> (6.14%) at a depth of  $\sim 1.56$   $\mu$ m in TiB<sub>2</sub> material, respectively.

### 2.3. Characterization

The morphology of the sample surface and Vickers indentation impression were recorded by scanning electron microscopy (SEM, Thermo Fisher Quanta FEG 250). In addition, the focused ion beam technology (Thermo Fisher, Helios G4 CX) was employed to lift up thin foils for the transmission electron microscopy (TEM) analysis. The thin foils were analyzed with a Talos F200X TEM at 200 kV in the bright-field mode, and a HV-1000 indentation test machine (Shanghai Lianer Testing Equipment Corporation) was used to perform the Vickers indentation tests.

### 3. Results and discussions

Before the SEM analysis, the composites were mechanically polished with diamond papers (from 800 to 12500 grit) until mirror-like surfaces were obtained. Fig. 2 shows the typical SEM images of the  $B_4C$ - $TiB_2$  composites with  $TiB_2$  volume fractions of 10.5% (Fig. 2(a)), 16.2% (Fig. 2(b)), and 29.8% (Fig. 2(c)). The white contrast indicated by black arrows in the SEM images are  $TiB_2$  phases, and the left, dark contrast represents  $B_4C$  grains. The  $TiB_2$  phases are distributed along the  $B_4C$  grain boundaries. With increasing  $TiB_2$  phase volume fraction, the fraction of isolated  $TiB_2$  particles decreases, and more and more  $TiB_2$  phases along the grain boundaries become connected, which results in an interconnected network from the two-dimensional (2D) point of view (Fig. 2(c)). Therefore, from the three-dimensional point of view, the  $TiB_2$  network forms a cage-like structure, which encapsulates the  $B_4C$  matrix grains. The average thickness of the  $TiB_2$  network of S3 is 0.9  $\mu m$ , and the statistical measurement based on the line-intercept method [20] reveals that the mean grain sizes of  $B_4C$  in the S1, S2, and S3 samples are 9.5, 8.6, and 6.4  $\mu m$ , respectively. Thus, the  $TiB_2$  fraction increases at the expense of consumed  $B_4C$ .

To evaluate the effect of the  $TiB_2$  network (cages) and its volume fraction on the heat transfer performance in the  $B_4C$ - $TiB_2$  composites, a series of numerical studies based on the typical microstructures of pure  $B_4C$  and  $B_4C$ - $TiB_2$  composites were implemented in the FE program

ABAQUS. The geometric constructions of the 2D pure  $B_4C$  and  $B_4C$ - $TiB_2$  composites FE model is shown in Fig. 3. A thermal continuity constraint was defined at each interface to connect the  $B_4C$  and  $TiB_2$  domains without heat dissipation. An initial temperature of 773 K was assigned to the entire computational region to simulate the reactor environment temperature, and 1273 K (boundary condition) was assigned to the left end of each model to generate a stable heater source; the other boundary conditions were adiabatic boundary conditions. The temperature dependence of the physical parameters of  $B_4C$  and  $TiB_2$  used in the numerical calculation are listed in Table 2 [18,21].

The temperature distributions used with different time scales for the pure  $B_4C$  and  $B_4C$ - $TiB_2$  composites models are shown in Fig. 4. The temperature distribution in pure  $B_4C$  is homogeneous along the vertical direction, and the isotherms are perpendicular to the horizontal axis. Whereas the temperature in the  $B_4C$ - $TiB_2$  composites presents an irregular gradient distribution. Furthermore, the temperature gradient in the  $B_4C$ - $TiB_2$  composites with a high  $TiB_2$  volume fraction is lower than that of the low  $TiB_2$  volume fraction. Particularly, the maximum temperature gradient appears in pure  $B_4C$ . Thus, heat is transmitted faster in the  $B_4C$ - $TiB_2$  composite than in the pure  $B_4C$ , the higher the volume fraction of  $TiB_2$ , the faster the heat transfers, which is consistent with the experimental results in [19].

To compare the heat transfer performance of the four structures quantitatively, the temperature variations at the middle point of the right-end boundary in each model are presented with respect to time in Fig. 5. The heating rate in the  $B_4C$ - $TiB_2$  composite with higher  $TiB_2$  volume fraction is higher than that of lower ones. For example, the temperature at point  $P_3$  in the  $B_4C$ - $TiB_2$  composite with the highest  $TiB_2$  volume fraction (29.8%) reaches 1181 K within 1  $\mu s$ , while the temperature at point  $P_0$  in the pure  $B_4C$  becomes only 1076 K within the same time. The FE analysis results demonstrate that the lower temperature gradient caused by the faster heat propagation in the  $B_4C$ - $TiB_2$  composites can be ascribed to the existence of the  $TiB_2$  network in the  $B_4C$  matrix, which has a higher thermal conductivity. If the composites are used as neutron-absorbing pellets in nuclear reactors, their high thermal conductance can rapidly cool the local high temperature caused by the nuclear reactions and greatly reduce the thermal stress caused by the thermal gradient, which reduces the risk of structural failure.

To further determine the equivalent average parameters and average heat conducting characteristics of the  $B_4C$ - $TiB_2$  composite, the equivalent homogeneous models with all the homogenized model parameters, such as conductivity, specific heat and density, determined by the volume-weighted-average were implemented for the three cases of

different  $\text{TiB}_2$  volume fractions (10.5%, 16.2% and 29.8%). Taking the temperature of the middle point of the right-end boundary as the assessment during simulation from 0.2 to 1  $\mu\text{s}$ , the comparison of the results calculated from real composite structure and equivalent homogeneous models are summarized in Table 3. It can be seen that the results of the equivalent homogeneous models are slightly overestimated for the three cases, but the maximum relative error is less than 5%, which indicates that the simple volume-weighted-average method can be used to roughly predict the equivalent parameters and average heat conducting characteristics of the  $\text{B}_4\text{C}$ – $\text{TiB}_2$  composite for variational volume fraction. It demonstrates the expected conductivity enhancement brought by the interconnectivity of the  $\text{TiB}_2$  phases as well.

In real nuclear reactors, the thermal gradient and He swelling-induced crack propagation in  $\text{B}_4\text{C}$  materials are mainly responsible for the disintegration of  $\text{B}_4\text{C}$  pellets in fast neutron reactors and in thermal neutron reactors, respectively. To investigate the effect of the  $\text{TiB}_2$  network (cages) on the crack propagation behavior in the  $\text{B}_4\text{C}$ – $\text{TiB}_2$  composites, Vickers indentation was employed to simulate the external stress that was applied to the  $\text{B}_4\text{C}$ – $\text{TiB}_2$  composites.

The typical Vickers indentation marks on the surfaces of S1, S2, and S3 are shown in Figs. 6(a), (b), and (c), respectively. The beginnings and endings of the cracks are indicated by double-headed arrows. Note that in



the Fig. 6(c), the gradient of sunken area is steep, outline of the Vickers indentation impression is irregular, but four cracks of the indentation are obvious. Therefore, each crack length is measured from the end of the crack, and along the inverse direction of crack propagation to the point where crack origins from the steeply sunken area (i.e. the indentation impression area). At a load of 9.8 N, the length of the cracks on S1 range from 20.7 to 27.9  $\mu\text{m}$ ; those on S2 and S3 range from 12.8 to 20.3  $\mu\text{m}$  and 6.8 to 13.5  $\mu\text{m}$ , respectively. The statistical results of the cracks show that the average values are  $22.9 \pm 2.8$ ,  $16.1 \pm 4.3$ , and  $12.2 \pm 3.8$   $\mu\text{m}$  for S1, S2, and S3, respectively. Fig. 7 presents the statistical results of the crack lengths on S1, S2, and S3, respectively. Evidently, the crack lengths decrease with increasing  $\text{TiB}_2$  volume fraction. Thereby the statistical results prove that the  $\text{TiB}_2$  phase distribution along the grain boundaries can impinge/block the crack propagation.

Figs. 8(a) and (b) present the enlarged SEM images of the crack propagation paths in S1 and S3, respectively. The white contrast in Figs. 8(a) and (b) are  $\text{TiB}_2$  phases: the  $\text{TiB}_2$  phases in Fig. 8(a) are isolated particles, which are distributed in the  $\text{B}_4\text{C}$  matrix; the  $\text{TiB}_2$  phases in Fig. 8(b) are interconnected, thereby forming a network (cages). The solid arrow in Fig. 8(a) indicates clearly that the propagating crack departs from its original straight trajectory and curves along the  $\text{B}_4\text{C}/\text{TiB}_2$  interface, thereby proving that the isolated  $\text{TiB}_2$  islands in the  $\text{B}_4\text{C}$  matrix

can redirect the crack propagation. A similar phenomenon was reported in [22]. In this study, the network (cages) topography in Fig. 8(b) clearly shows that the crack propagates through the  $\text{TiB}_2$  walls (dashed arrows 2 and 3) and extends along the interface between the  $\text{B}_4\text{C}$  and  $\text{TiB}_2$  phases (dashed arrow 1), which facilitates the energy release of the crack tip. This is confirmed by the shorter crack length ( $12.2 \pm 3.8 \mu\text{m}$ ) of S3 than those of S1 ( $22.9 \pm 2.8 \mu\text{m}$ ) and S2 ( $16.1 \pm 4.3 \mu\text{m}$ ), as shown in Fig. 6.

It can be concluded that there are two underlying ways in which the  $\text{TiB}_2$  phases affect the crack propagation in  $\text{B}_4\text{C}$ – $\text{TiB}_2$  composites: first, when the volume fraction of the  $\text{TiB}_2$  phase is low,  $\text{TiB}_2$  distributes in the  $\text{B}_4\text{C}$  matrix as isolated particles (shown in Fig. 8(a)), and when the propagation of a crack tip encounters a  $\text{TiB}_2$  particle, the crack moves along the  $\text{B}_4\text{C}/\text{TiB}_2$  interface, prolongs the crack propagation length and dissipates more energy, finally results in an improvement of the fracture toughness of the  $\text{B}_4\text{C}$ – $\text{TiB}_2$  composites. Similar dissipation mechanisms at the  $\text{B}_4\text{C}/\text{TiB}_2$  interfaces are also found in Refs. [23, 24]. Second, when the volume fraction of the  $\text{TiB}_2$  phase is high, the  $\text{TiB}_2$  phase forms an enclosed cage-like structure that encapsulates the  $\text{B}_4\text{C}$  grains (Fig. 8(b)). Thus, the cracks have to penetrate the  $\text{TiB}_2$  walls before extending along the  $\text{B}_4\text{C}/\text{TiB}_2$  interfaces or must propagate through the neighboring  $\text{B}_4\text{C}$  grains. According to the model of Cook et al. on crack propagation in brittle systems [25], additional energy is required to deflect the crack

propagation and initiate secondary crack propagation across the interface;  
the primary crack requires much energy.

To quantitatively measure the fracture toughness of the B<sub>4</sub>C-TiB<sub>2</sub> composites, following equations are used [26]:

$$K_{IC} = 0.016(E/H_V)^{0.5}Pc^{-1.5}, \quad (4)$$

where

$$H_V = \frac{1.8544 \times P}{4a^2 \times 1000}, \quad (5)$$

in which  $E$  is the Young's modulus,  $H_V$  the Vickers hardness,  $P$  the Vickers indentation load, and  $a$  and  $c$  are the half length of the residual Vickers indenter impression diagonal and half length of the radial crack diagonal, respectively. The fracture toughness of the composites  $K_{IC}$  were calculated to be  $3.06 \pm 0.28$  (MPa·m<sup>1/2</sup>),  $3.81 \pm 0.33$ (MPa·m<sup>1/2</sup>), and  $4.38 \pm 0.67$  (MPa·m<sup>1/2</sup>) for S1, S2, and S3, respectively. In other words, increasing the TiB<sub>2</sub> volume fraction and optimizing the distribution of TiB<sub>2</sub> can impinge/block the propagation of cracks and improve the fracture toughness of the B<sub>4</sub>C-TiB<sub>2</sub> composites. This promotes the integration of B<sub>4</sub>C pellets and improves the CR performance in the harsh environments of nuclear reactors.

He behavior of the composites under irradiation conditions is important for the evaluation of the composites serving in the reactors, however, it was seldomly studied. Therefore, we conducted He ions irradiation on the composites and initially investigated the He behavior by

TEM observation.

The TEM images in Fig. 9 show the He bubble distribution and morphology in B<sub>4</sub>C phase of samples S1, S2, and S3. The images were recorded with the same underfocus of 2.8  $\mu\text{m}$ . The He bubbles, which are small bright dots in the images, are located within a band area. The width of He bubbles deposition band is smaller than that of the implanted band as calculated by SRIM, similar phenomenon is observed by Motte et al. [8]. It is suggested that this is due to the different depths of the He ions induced damage profile and the He ions implanted profile. In the area of the damage profile, lot of vacancies were introduced by energetic ions collision, while in the area of He atoms implanted band, He atoms greatly outnumbered the vacancies. In the overlapped areas (the width of which was smaller than the implanted band as calculated by SRIM), abundant vacancies and He atoms promoted the formation of He-vacancy clusters and increased the density of He bubble germs. After annealing, He-vacancy clusters evolved into visible He bubbles under TEM observation and formed a bubbles band in the overlapped area. Moreover, Gillet et al. found that the dissociation energy of He-vacancy is  $\sim 2$  eV, the high energy barrier inhibited the He diffusion by the formation of He-vacancy clusters [27], and this explained that no He bubbles outside the band area can be found (excepted the He bubbles in the grain boundaries).

The He bubbles in the bubbles band are small and dense; such feature has been argued to arise partially from the diffusion behavior of He atoms in  $B_4C$ . According to Refs. [27-30], He atoms must overcome a high energy barrier to migrate even through the most probable migration paths owing to the intrinsic chemical bond and lattice structure of  $B_4C$ . Schneider et al. discovered that He atoms prefer to migrate between  $\langle 111 \rangle$  planes by first-principle calculations. Moreover, they discovered that the activation energy of He ion diffusion is approximately 2 eV [28], which is consistent with the experimental results in [30]. The 2 eV migration energy means that the aggregation of He atoms in  $B_4C$  materials is retarded and explains the observation of small-sized He bubbles in this study rather than large-sized He bubbles in metals under similar irradiation conditions [31].

The He bubbles that are distributed along the interfaces are bigger than the bubbles distributed in the  $B_4C$  and  $TiB_2$  grains (however, bubbles along the  $TiB_2$ – $TiB_2$  interface are not investigated in this study), as shown in Fig. 10. This is due to the special structure of the interface. Misfits in the lattice structure of the interfaces contain plenty of open volume [32], which provides adequate free space for the deposition of irradiation-induced point defects (e.g., vacancies, interstitials, transmuted elemental atoms) [33]. Owing to the high binding energy between vacancies and He atoms ( $\sim 2$  eV [27,28]), the open volume of interfaces

can act as efficient trapping sites for He and preferential nucleation sites for He bubbles [8,9,34]. Therefore, once the He atoms are captured by the interfaces, they cannot easily be released within the temperature range investigated in this study. As shown in Fig. 10, no He bubbles depleted zone was detected, which is consistent with the results of Motte et al.'s work [28] that it was hard for He atoms to diffuse through or in the  $B_4C$  grain boundaries below 1373 K. This might prove that long-range He diffusion is negligible at 1273 K. Moreover, TEM image in Fig. 10 shows that He bubbles deposition band in  $B_4C$  is closer to the surface than that in  $TiB_2$ , this phenomenon is also consistent with SRIM calculation as shown in Fig. 1 that the overlap of He distribution and damage profile is shallower in  $B_4C$  than that in  $TiB_2$ .

In a realistic environment of nuclear reactors, increasing the density of sinks for the precipitation of He atoms is an effective way to suppress the formation of large He bubbles [35], and reduce the He-induced property degradation (e.g. He embrittlement). Therefore, the network (cages) of the  $TiB_2$  phases provides numerous sinks for He precipitation, which might inhibit the formation of large He bubbles, and mitigate the effects of He-accumulation-induced shear stress at interfaces, and the resulting microcracks, especially in the thermal neutron reactors. However, other factors may affect performance of the  $B_4C$ - $TiB_2$  composites, such as shear stress induced by He accumulation at the

419 interfaces, different thermal dilation between  $B_4C$  and  $TiB_2$ . To have a  
420 better evaluation of the  $B_4C$ – $TiB_2$  composites in a realistic environment, a  
421 detailed numerical evaluation will be carried out in the future study.

422 As an important component of the  $B_4C$ –diborides composites, the  
423 behavior of diborides under irradiation environment is very crucial to the  
424 performance of composites. Cheminant et al. conducted neutron  
425 irradiation on  $HfB_2$ , and found that porosity appeared at grain boundaries,  
426 and resulted in a decrease of the thermal diffusivity [36], which lead to  
427 the degradation of  $B_4C$ – $HfB_2$  composites. Regarding the  $TiB_2$  in this  
428 study, despite the inimitable merits of  $TiB_2$ , however, its irradiation  
429 behavior was seldomly studied, which is very important for the  
430 application of  $TiB_2$  as neutron absorbers. To the best of our knowledge,  
431 only two studies reported the microstructural evolution of  $TiB_2$  under  
432 irradiation conditions [37, 38]. Therefore, a systematic study on the  
433 irradiation tolerance of  $TiB_2$  is needed, which will be part of our future  
434 work.

### 435 3. Conclusion

436 To improve the performance of  $B_4C$  neutron absorption material in  
437 nuclear reactors, a set of property-optimized  $B_4C$ – $TiB_2$  composites were  
438 designed and fabricated through a combination of the molten-salt and  
439 SPS methods. The  $TiB_2$  phase distributes along the  $B_4C$  grain boundaries  
440 and forms a connected network (cages), which encapsulates the  $B_4C$

matrix phase. The thermal conductivity and fracture toughness of the  $B_4C$ - $TiB_2$  composites are greatly improved owing to the special cage-like structure. The FE analyses show that the connected  $TiB_2$  network promotes the heat transfer and improves effectively the overall thermal conductivity of the  $B_4C$ - $TiB_2$  composite. The improved thermal conductivity results in a lower thermal stress, which mitigates thermal-stress-induced crack propagation.

Vickers indentation tests were performed on the composites to study the crack propagation behavior. The  $TiB_2$  network (cages) can effectively impinge/block the crack propagation, thereby improving the composite fracture toughness. This is important for maintaining the integration of  $B_4C$ - $TiB_2$  composites if the composite serves as neutron absorption material in nuclear reactors.

Moreover, He ion irradiation was used to investigate the He behavior in the composites and to simulate the situation in which a high quantity of He is produced by the  $B^{10}(n, \alpha) Li^7$  nuclear reaction. The TEM results show that the interfaces of  $B_4C$  and  $TiB_2$  are effective trapping sites for He atoms and nucleation sites for He bubbles. Note that in a fast neutron reactor, the ballistic damage induced by energetic neutrons scattering and the nuclear reaction products (e.g., He, Li) scattering are much higher than the sole He ions implantation, this leads to a higher vacancy/He ratio and the possible consequences on the defects dynamics [28].



Overall, this study provides a synthesis method for fabricating neutron absorption materials for the application in nuclear reactors. The special property-optimized  $B_4C$ - $TiB_2$  composites with designed microstructure exhibit a better resistance to disintegration under irradiation and in the thermodynamic environment of nuclear reactors. In addition, they have a great potential for the application as neutron-absorbing pellets in nuclear reactors.

In the future study, other issues will be addressed to have a comprehensive evaluation of  $B_4C$ - $TiB_2$  composites under irradiation conditions. For example, helium behavior in  $TiB_2$  and irradiation resistant property of  $TiB_2$ , effects of the special cage-like structure and  $TiB_2$  content on He diffusion and release during annealing, other synthesis routes to optimize the structure and properties of the  $B_4C$ - $TiB_2$  composites, influence of He bubbles aggregation along the  $B_4C$ - $TiB_2$  and  $TiB_2$ - $TiB_2$  interface on the thermal conductivity of the composites and the crack propagation behavior, etc.

#### Acknowledgements

This research was supported by the National Natural Science Foundation of China (No. 11902129, 11805245), Strategic Priority Research Program of Chinese Academy of Sciences (No. XDA21010202), Natural Science Fund of Zhejiang Province (No. LQ20A050001), Natural Science Fund of Ningbo City (No. 2019A610183), and China

485 Postdoctoral Science Foundation (2019T120963).

486 Data availability

487 The raw data required to reproduce these findings cannot be shared at  
488 this time as the data is part of an ongoing study. The processed data  
489 required to reproduce these findings cannot be shared at this time as the  
490 data is part of an ongoing study.

491 References

492 [1] T. Donomae, K. Maeda, Fast Spectrum Control Rod Materials, in:  
493 R.J.M. Konings, T.R. Allen, R.E. Stoller, S. Yamanaka (Eds.),  
494 Comprehensive nuclear materials, Elsevier, Netherlands, 2012, pp.  
495 509-534.

496 [2] T. Maruyama, S. Onose, T. Kaito, H. Horiuchi, J. Nucl. Sci. Technol.  
497 34 (10) (1997) 1006-1014.

498 [3] N. Moncoffre, N. Toulhoat, N. Bererd, Y. Pipon, G. Silbermann, A.  
499 Blondel, N. Galy, P. Sainsot, J.-N. Rouzaud, D. Deldicque, V. Dauvois, J.  
500 Nucl. Mater. 472 (2016) 252-258.

501 [4] V. Kerleguer, C. Jegou, L. D. Windt, V. Broudic, G. Jouan, S. Miro, F.  
502 Tocino, C. Martin, J. Nucl. Mater. 529 (2020) 151920.

503 [5] D. Gosset, Absorber materials for generation IV reactors, in: P. Yvon,  
504 Structural Material for Generation IV Nuclear reactors, Elsevier,  
505 Netherlands, 2017, pp. 533-567.

506 [6] IAEA-TECDOC-1132, Control Assembly Materials for Water

- 507 Reactors: Experience, Performance and Perspectives, 1998.
- 508 [7] G.W. Hollenberg, J.A. Basmajian, J. Am. Ceram. Soc. 65 (4) (1982)
- 509 179-181.
- 510 [8] V. Motte, D. Gosset, G. Gutierrez, S. Doriot, N. Moncoffre, J. Nucl.
- 511 Mater. 514 (2019) 334-347.
- 512 [9] T. Stoto, J. Ardonneau, L. Zuppiroli, M. Castiglioni, B. Weckermann,
- 513 Radiat. Eff., 105 (1987) 17-30.
- 514 [10] R. M. Horn, B. D. Frew, P. V. Diemen, Thermal Spectrum Control
- 515 Rod Materials, in: R.J.M. Konings, T.R. Allen, R.E. Stoller, S. Yamanaka
- 516 (Eds.), Comprehensive nuclear materials, Elsevier, Netherlands, 2012, pp.
- 517 485-507.
- 518 [11] D. Gosset, M. Colin, Tech. Ing. BN3720 (2007).
- 519 [12] G.M. Decroix, D. Gosset, B. Kryger, M. Boussuge, H. Burlet,
- 520 Improvement of thermomechanical properties of ceramic materials for
- 521 nuclear applications, in: P. Vincenzini (Ed.), 8th CIMTEC, Florence, Italy,
- 522 1994.
- 523 [13] K. Sairam, J.K. Sonber, T.S.R.Ch. Murthy, C. Subramanian, R.C.
- 524 Hubli, A.K. Suri, Int. J. Ref. Met. Hard Mater. 35 (2012) 32-40.
- 525 [14] J. Matsushita, T. Suzuki, A. Sano, J. Ceram. Soc. Jpn. 101 (9) (1993)
- 526 1074-1077.
- 527 [15] B. Basu, G.B. Raju, A.K. Suri, Int. Mater. Rev. 51 (6) (2006) 352-
- 528 374.

- 529 [16] Z.H. Zhang, X.B. Shen, F.C. Wang, S.K. Lee, Q.B. Fan, M.S. Cao,  
530 Scr. Mater. 66 (3–4) (2012) 167–170.
- 531 [17] C. Subramanian, T.S.R.C. Murthy, A.K. Suri, Int. J. Refract. Met.  
532 Hard Mater. 25 (4) (2007) 345–350.
- 533 [18] R.G. Munro, J. Res. Natl. Inst. Stand. Technol. 105(2000)709-720.
- 534 [19] D.L. Ren, Q. Deng, J. Wang, J.S. Yang, Y.B. Li, J.Q. Shao, M. Li, J.  
535 Zhou, S.L. Ran, S.Y. Du, Q. Huang, J. Am. Ceram. Soc. 101 (2018) 1–7.
- 536 [20] J.C. Wurst, J.A. Nelson, J. Am. Ceram. Soc. 55 (2) (1972) 109.
- 537 [21] P.A. Medwick, H.E. Fischer, R.O. Pohl, J. All. Comp. 203 (1994)  
538 67-75.
- 539 [22] S. Yamada, K. Hirao, Y. Yamauchi, S. Kanzaki, J. Eur. Ceram. Soc.  
540 23 (2003) 1123-1130.
- 541 [23] Y. Zhu, H.W. Cheng, Y.W. Wang, R. An, J. All. Comp. 772 (2019)  
542 537-545.
- 543 [24] M.S. Heydari, H.R. Baharvandi, K. Dolatkhah, Int. J. Refract. Met.  
544 Hard Mater. 51 (2015) 6-13.
- 545 [25] J. Cook, J. E. Gordon, C. C. Evans, D. M. Marsh, Proc. R. Soc. Lond.  
546 A 282(1964)508-520.
- 547 [26] G.R. Anstis, P. Chantikul, B.R. Lawn, D.B. Marshall, J. Am. Ceram.  
548 Soc. 64 (1981) 533-538.
- 549 [27] K. Gillet, G. Roma, J.P. Crocombette, D. Gosset, J. Nucl. Mater. 512  
550 (2018) 288-296.

- 551 [28] V. Motte, D. Gosset, T. Sauvage, H. Lecoq, N. Moncoffre, J. Nucl.  
552 Mater. 517 (2019) 165-174.
- 553 [29] A. Schneider, G. Roma, J.P. Crocombette, V. Motte, D. Gosset, J.  
554 Nucl. Mater. 498 (2017) 157-162.
- 555 [30] D. Horlait, D. Gosset, A. Jankowiak, V. Motte, N. Lochet, T. Sauvage,  
556 E. Gilabert, J. Nucl. Mater. 527(2019)151834.
- 557 [31] M.H. Cui, J. Wang, Z.G. Wang, T.L. Shen, K.F. Wei, C.F. Yao, J.R.  
558 Sun, N. Gao, Y.B. Zhu, L.L. Pang, D. Wang, H.P. Zhu, Y. Han, X.S. Fang,  
559 Nucl. Instrum. Methods Phys. Res., Sect. B 406 (2017) 611-617.
- 560 [32] Ilya A. Ovid'ko, Rev. Adv. Mater. Sci. 1 (2000) 61-107.
- 561 [33] I.J. Beyerlein, A. Caro, M.J. Demkowicz, N.A. Mara, A. Misra, B.P.  
562 Uberuaga, Mater. Today 16 (2013) 443-449.
- 563 [34] D. Gosset, P. Herter, V. Motte, Nucl. Instrum. Methods Phys. Res.,  
564 Sect. B 434 (2018) 66-72.
- 565 [35] P.D. Edmondson C.M. Parish, Y. Zhang, A. Hallen, M.K. Miller,  
566 Scripta Mater. 65 (2011) 731-734.
- 567 [36] P. Cheminant, X. Deschanel, L. Boulanger, A. Thorel, Key Eng.  
568 Mater. 132-136 (1997) 643-646.
- 569 [37] M. Carrard, D. Emin, L. Zuppiroli, Phys. Rev. B 51 (1995)  
570 11270-11274.
- 571 [38] A. Bhattacharya, C.M. Parish, T. Koyanagi, C.M. Petrie, D. King, G.  
572 Hilmas, W.G. Fahrenholtz, S.J. Zinkle, Y. Katoh, Acta Mater. 165 (2019)

573 26-39.

574

575 Figure captions

576 Fig. 1. Displacement damage and He concentration as a function of  
577 penetration depth in  $B_4C$  and  $TiB_2$  material, respectively.

578 Fig. 2. SEM images of surface morphology of (a) 10.5 Vol.%  $TiB_2$   
579 composites, (b) 16.2 Vol.%  $TiB_2$  composites, and (c) 29.8 Vol.%  $TiB_2$   
580 composites; arrows indicate the  $TiB_2$  phases.

581 Fig. 3. Geometric construction and boundary conditions of FE models: (a)  
582 pure  $B_4C$  model; (b)-(d)  $B_4C$ - $TiB_2$  composite model based on SEM  
583 image of sample S1, S2 and S3, respectively; light and dark contrasts  
584 represent  $TiB_2$  network and  $B_4C$  matrix, respectively;  $P_i$  ( $i=0, 1, 2$  and  $3$ )  
585 represents middle point of the right-end boundary of each calculated  
586 domain.

587 Fig. 4. Temperature distribution in pure  $B_4C$  and  $B_4C$ - $TiB_2$  composites  
588 with different  $TiB_2$  volume fractions at different time scales calculated by  
589 FE method: (a) pure  $B_4C$ ; (b)-(d)  $B_4C$ - $TiB_2$  composites of sample S1, S2  
590 and S3, respectively.

591 Fig. 5. Temperature variation at points  $P_i$  (center of the right-end  
592 boundary in each model) with respect to time.

593 Fig. 6. Typical Vickers indentation impressions on (a) 10.5 Vol.%  $TiB_2$   
594 composites, (b) 16.2 Vol.%  $TiB_2$  composites, and (c) 29.8 Vol.%  $TiB_2$

composites. The double arrows indicate the starting to the ending of the cracks.

Fig. 7. Statistical results of Vickers indentation-induced crack length for different  $\text{TiB}_2$  volume fractions of composites.

Fig. 8. SEM images of Vickers indentation-induced crack propagation; solid arrows in (a) indicate deflection of cracks by isolated  $\text{TiB}_2$  particles, and dashed arrows in (b) indicate crack penetration through  $\text{TiB}_2$  cages.

Fig. 9. TEM images of He bubble morphology in He deposition band in  $\text{B}_4\text{C}$  phase of (a) 10.5 Vol.%  $\text{TiB}_2$  composites, (b) 16.2 Vol.%  $\text{TiB}_2$  composites, and (c) 29.8 Vol.%  $\text{TiB}_2$  composites.

Fig. 10. TEM image of He bubble morphology in He deposition band and at  $\text{B}_4\text{C}$ – $\text{TiB}_2$  interfaces. The arrows indicate the incident direction of He ions. The dash lines indicate the boundaries of He bubbles band.

Table 1. Molar ratio of raw  $\text{B}_4\text{C}$  powder and Ti powder for molten-salt reaction, volume fraction of  $\text{TiB}_2$ , weight percent of  $\text{TiB}_2$ ,  $\text{B}_4\text{C}$  and C in synthesized bulks.

Samples	Molar ratio ( $\text{B}_4\text{C}:\text{Ti}$ )	Volume fraction of $\text{TiB}_2$	Weight percent of $\text{TiB}_2$	Weight percent of $\text{B}_4\text{C}$	Weight percent of C
S1	6:1	10.5%	18.0%	80.4%	1.6%
S2	4:1	16.2%	26.0%	72.0%	2.0%
S3	2:1	29.8%	44.0%	52.0%	4.0%

Table 2. Material properties of  $\text{B}_4\text{C}$  and  $\text{TiB}_2$  used in heat transfer

613

analysis [16, 19]

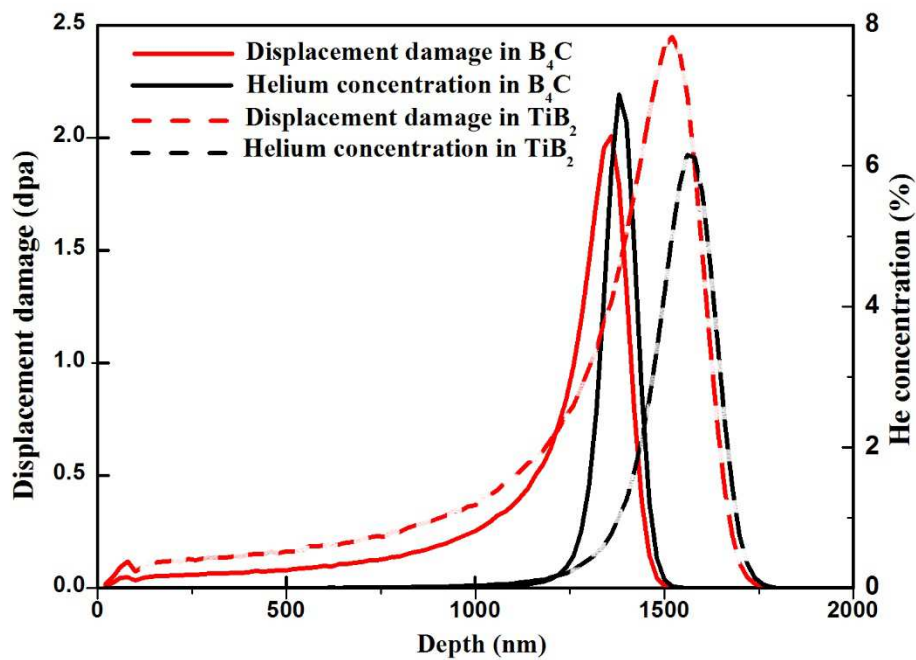
Temperature (K)	Conductivity ( $\text{W} \cdot \text{m}^{-1} \cdot \text{K}^{-1}$ )		Specific Heat ( $\text{J} \cdot \text{kg}^{-1} \cdot \text{K}^{-1}$ )		Density ( $\text{kg/m}^3$ )	
	773	1273	773	1273	773	1273
$\text{B}_4\text{C}$	20.00	11.00	1680.80	2072.68	2550	2550
$\text{TiB}_2$	81.00	78.10	1073.00	1186.00	4450	4390

614

615 Table 3. Comparison of the results calculated from real composite  
 616 structure models (CM), equivalent homogeneous models (HM) and the  
 617 relative error (RE).

Time ( $\mu\text{s}$ )	S1			S2			S3		
	CM(K)	HM(K)	RE(%)	CM(K)	HM(K)	RE(%)	CM(K)	HM(K)	RE(%)
0.2	819	836	2.1	832	856	2.9	867	901	3.9
0.4	917	948	3.4	941	981	4.3	997	1043	4.6
0.6	996	1033	3.7	1024	1069	4.4	1093	1129	4.2
0.8	1057	1093	3.7	1085	1128	4.0	1142	1180	3.3
1	1102	1137	3.2	1130	1168	3.4	1181	1212	2.6

618



619



Fig. 1. Displacement damage and He concentration as a function of penetration depth in  $B_4C$  and  $TiB_2$  material, respectively.

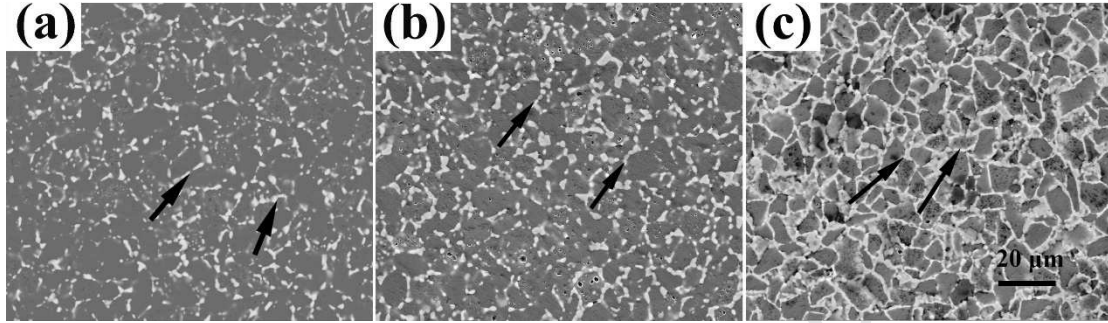


Fig. 2. SEM images of surface morphology of (a) 10.5 Vol.%  $TiB_2$  composites, (b) 16.2 Vol.%  $TiB_2$  composites, and (c) 29.8 Vol.%  $TiB_2$  composites; arrows indicate the  $TiB_2$  phases.

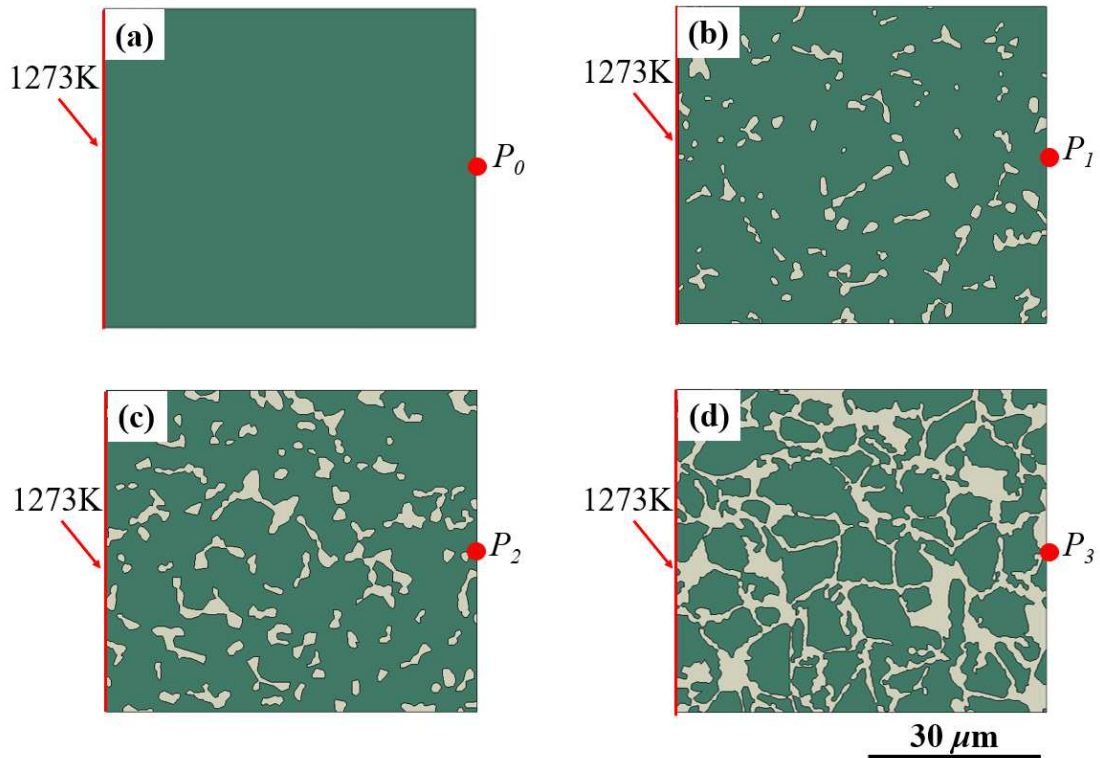


Fig. 3. Geometric construction and boundary conditions of FE models: (a) pure  $B_4C$  model; (b)-(d)  $B_4C$ - $TiB_2$  composite model based on SEM

image of sample S1, S2 and S3, respectively; light and dark contrasts represent  $\text{TiB}_2$  network and  $\text{B}_4\text{C}$  matrix, respectively;  $P_i$  ( $i=0, 1, 2$  and  $3$ ) represents middle point of the right-end boundary of each calculated domain.

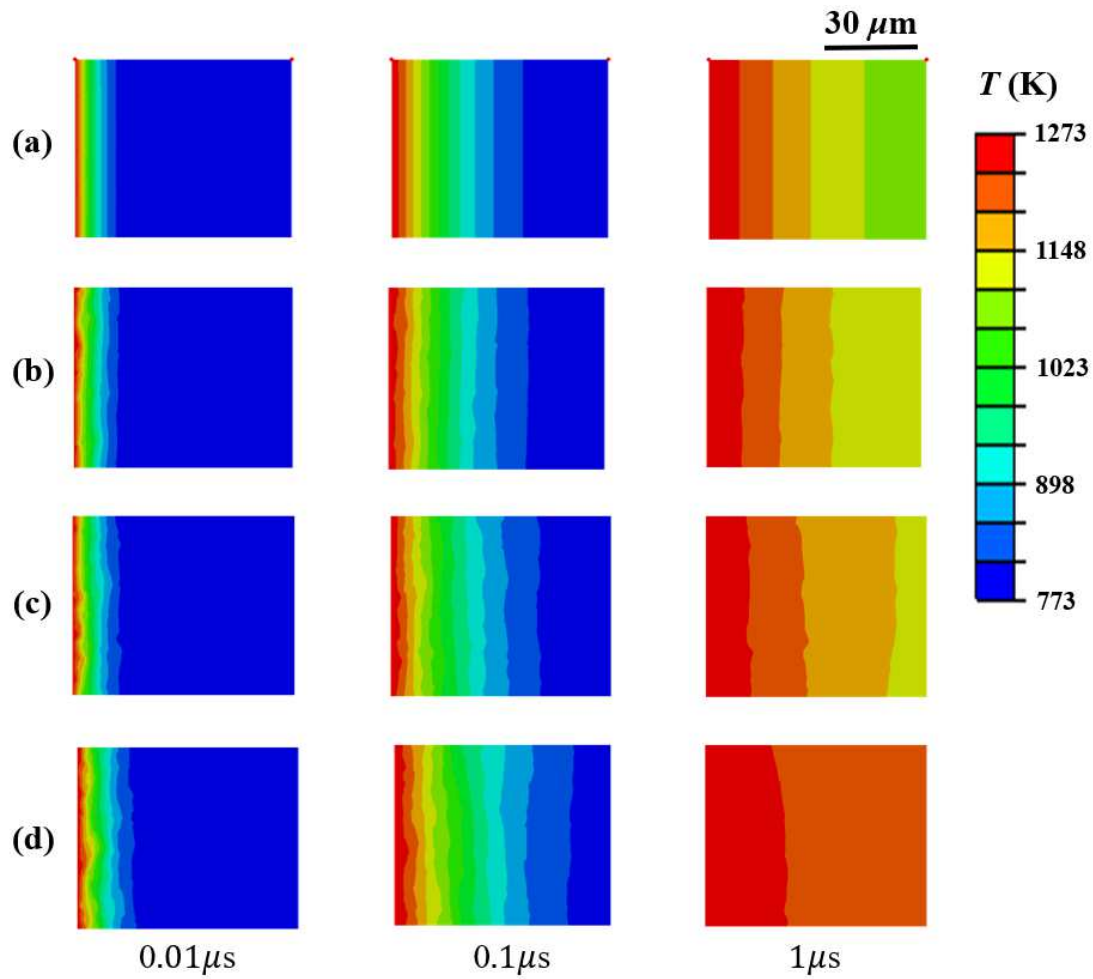


Fig. 4. Temperature distribution in pure  $\text{B}_4\text{C}$  and  $\text{B}_4\text{C-TiB}_2$  composites with different  $\text{TiB}_2$  volume fractions at different time scales calculated by FE method: (a) pure  $\text{B}_4\text{C}$ ; (b)-(d)  $\text{B}_4\text{C-TiB}_2$  composites of sample S1, S2 and S3, respectively.

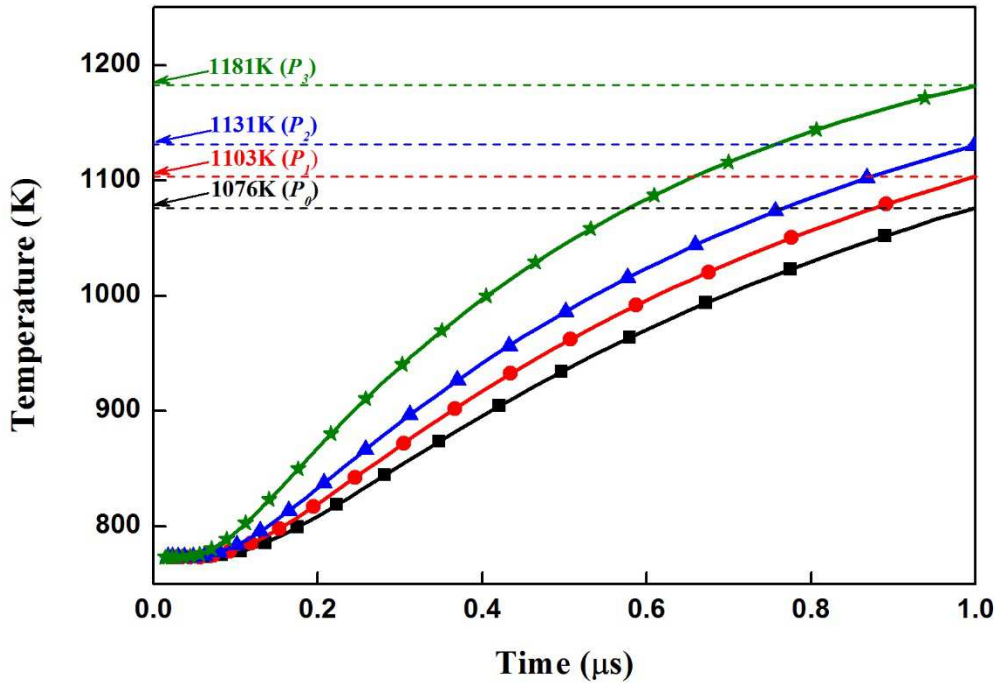


Fig.5. Temperature variation at points  $P_i$  (center of the right-end boundary in each model) with respect to time.

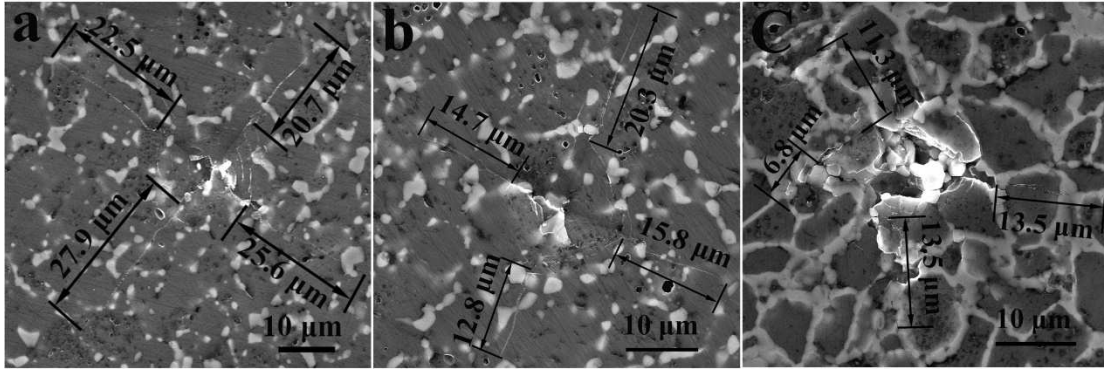


Fig. 6. Typical Vickers indentation impressions on (a) 10.5 Vol.%  $\text{TiB}_2$  composites, (b) 16.2 Vol.%  $\text{TiB}_2$  composites, and (c) 29.8 Vol.%  $\text{TiB}_2$  composites. The double arrows indicate the starting to the ending of the cracks.

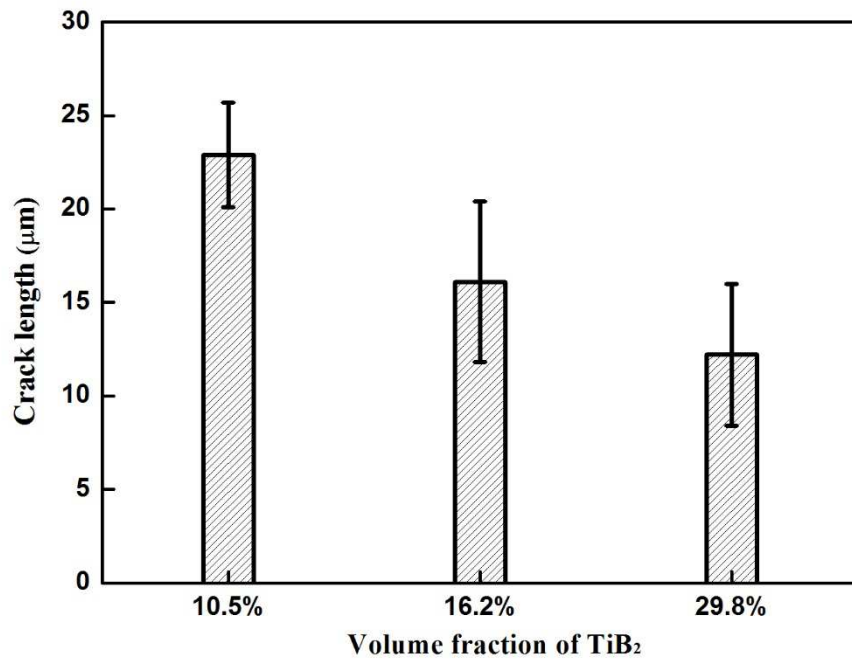


Fig. 7. Statistical results of Vickers indentation-induced crack length for different  $\text{TiB}_2$  volume fractions of composites.

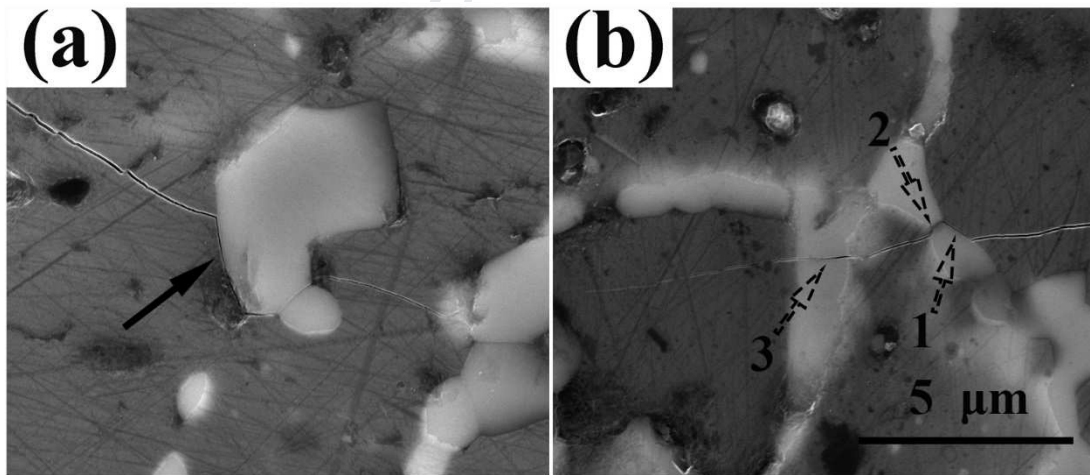


Fig. 8. SEM images of Vickers indentation-induced crack propagation; solid arrows in (a) indicate deflection of cracks by isolated  $\text{TiB}_2$  particles, and dashed arrows in (b) indicate crack penetration through  $\text{TiB}_2$  cages.



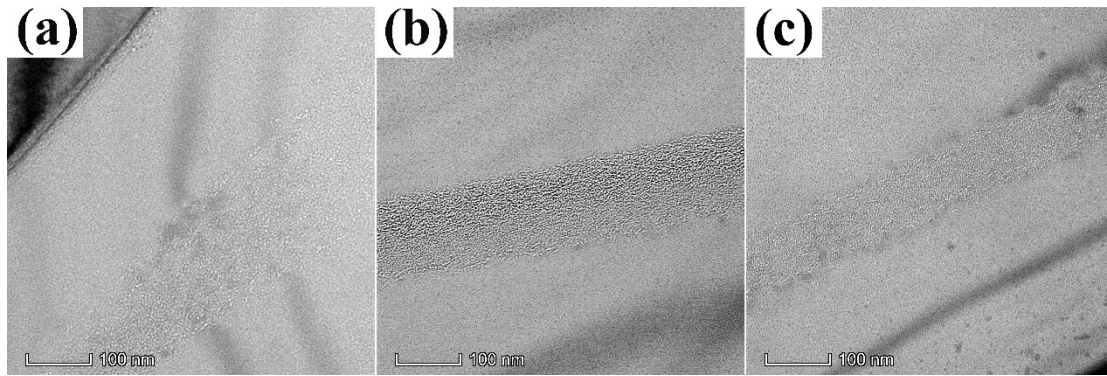


Fig. 9. TEM images of He bubble morphology in He deposition band in  $B_4C$  phase of (a) 10.5 Vol.%  $TiB_2$  composites, (b) 16.2 Vol.%  $TiB_2$  composites, and (c) 29.8 Vol.%  $TiB_2$  composites.

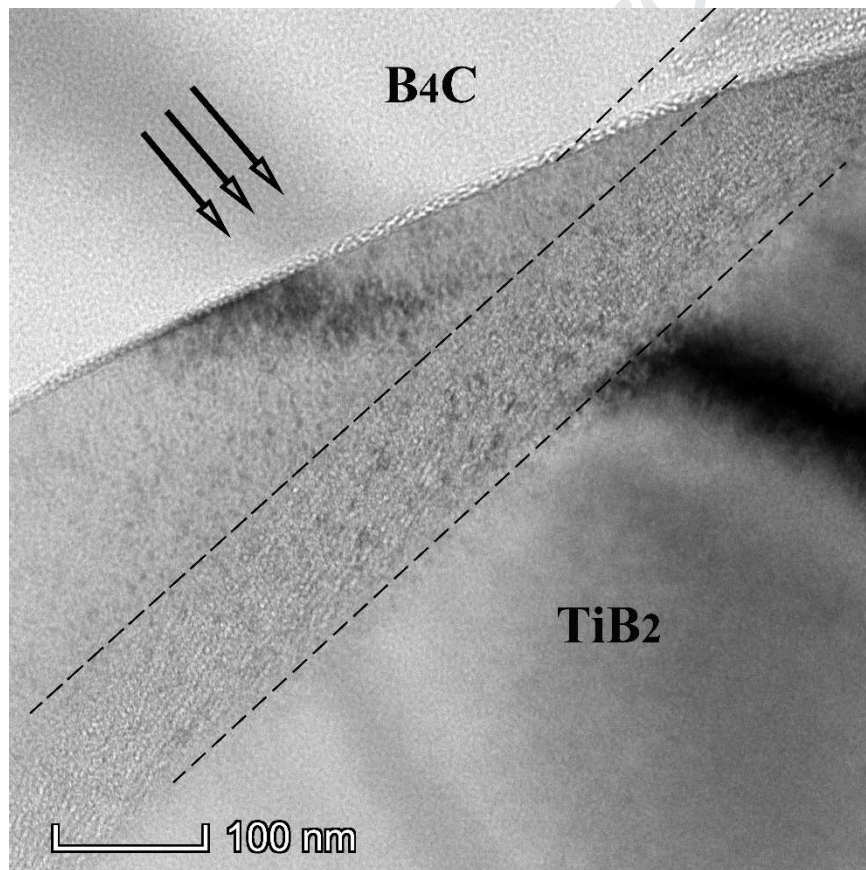


Fig. 10. TEM image of He bubble morphology in He deposition band and at  $B_4C$ - $TiB_2$  interfaces. The arrows indicate the incident direction of He ions. The dash lines indicate the boundaries of He bubbles band.

$B_4C$ - $TiB_2$  composites with  $B_4C$  grains encapsulated by  $TiB_2$  network (cages) are fabricated.

$TiB_2$  network (cages) greatly improve thermal conductivity and fracture toughness of  $B_4C$ - $TiB_2$  composites.

The interconnected interfaces between  $TiB_2$  network (cages) and  $B_4C$  grains act as effective sinks for the aggregation of He atoms.

**Declaration of interests**

☒ The authors declare that they have no known competing financial interests or personal relationships that could have appeared to influence the work reported in this paper.

☐ The authors declare the following financial interests/personal relationships which may be considered as potential competing interests: